Photoelectrons on closed crustal field lines at Mars

Matthew Trantham,[1] Mike Liemohn,[1] David Mitchell,[2] and Jacki Frank[1]

[1]   A statistical survey of dayside photoelectrons in the Mars upper ionosphere is presented and discussed. A methodology for isolating photoelectron spectra on strong crustal field lines is developed and used to obtain a database of over 280,000 distributions from the Mars Global Surveyor (MGS) electron reflectometer instrument. The relationship of these electron fluxes to various controlling factors is explored and presented. It is found that much of the flux variation can be explained by a linear fit with the EUV solar radiation proxy, adjusted for the Sun-Mars distance and local solar zenith angle. The state of the lower atmosphere seems to also play a critical role in the photoelectron flux intensity. An interval with a global dust storm shows an increased flux and steepened slope for the relationship with EUV radiation. This implies that the dust storm is altering the density, composition, and/or temperature of the photoelectron source region within the thermosphere and perhaps even the characteristics of the Mars exosphere above the MGS orbit. Other parameters considered had either no influence or a small perturbation compared to this dominant trend.

Citation: Trantham, M., M. Liemohn, D. Mitchell, and J. Frank (2011), Photoelectrons on closed crustal field lines at Mars, *J. Geophys. Res.*, *116*, A07311, doi:10.1029/2010JA016231.

1. Introduction

[2]   At some point, in Mars' ancient history, the planet possessed a much thicker atmosphere capable of sustaining liquid water. In contrast, today the atmosphere is thin, and no longer capable of maintaining liquid water on the surface. A definitive explanation of how and why this transformation took place is a topic of great debate and interest. One explanation proposes that liquid water froze and remains largely on the Martian surface [*Carr and Schaber*, 1977; *Rossbacher and Judson*, 1981]. Another theory suggests that much of the atmosphere could have escaped to space [*Chassefiere and Leblanc*, 2004]. This study focuses on the latter, and what parameters affect photoelectron fluxes which could be used to estimate the rate of atmospheric loss.

[3]   There are four basic methods for atmospheric escape: Jeans escape, dissociative recombination, ion escape and ionospheric outflow, and sputtering [*Chassefiere and Leblanc*, 2004]. Jeans escape [*Jeans*, 1904] primarily affects light elements and is inefficient at removing other heavier elements. Dissociative recombination contributes to atmospheric escape when an ion recombines with an electron forming energetic neutrals that can escape Mars [*McElroy and Donahue*, 1972]. Ion escape occurs when a neutral is ionized by UV, electron impact or charge exchange and picked up by the solar wind [*Luhmann and Kozyra*, 1991]. Ionospheric outflow can also

be an important loss mechanism for ions created below the ionopause [*Luhmann and Kozyra*, 1991; *Kar et al.*, 1996] . Sputtering is the final major mechanism of atmospheric escape. It occurs when heavy ions picked up by the solar wind impact with the neutral atmosphere. Due to their energization from the pickup process while in the solar wind, they create a backsplash from the atmosphere, giving some neutrals the energy needed to escape [*Luhmann and Kozyra*, 1991; *Luhmann et al.*, 1992]. However, estimates of escape rates for these processes vary by orders of magnitude [*Chassefiere and Leblanc*, 2004; *Barabash et al.*, 2007; *Lundin et al.*, 2008].

[4]   This wide range of estimates stems from two major problems, insufficient understanding of the space environment at Mars and an overall deficiency of neutral and ion measurements at Mars. These two issues are likely related; therefore it is useful to carefully exam the available data sets in order to get the most information out of them. One available data set is suprathermal electrons, which have been measured by electrostatic analyzers on several Mars missions. In particular, the combination of Mars Global Surveyor (MGS) and Mars Express provide a nearly continuous time series of suprathermal electron flux measurements from 1997 to present. The question, therefore, is whether it is possible to extract information about atmospheric escape from suprathermal electron measurements.

[5]   *Liemohn et al.* [2006a] and *Frahm et al.* [2006a] showed that photoelectrons in Mars' tail are magnetically connected to the dayside ionosphere. A pair of follow-on studies by *Liemohn et al.* [2006b] and *Frahm et al.* [2006b] further quantified when and where within the Mars magnetotail atmospheric photoelectrons are observed. *Liemohn et al.* [2006b] also suggests that dayside photoelectron intensities could be used as a proxy for the ion escape

[1]Department of Atmospheric, Oceanic, and Space Sciences, University of Michigan, Ann Arbor, Michigan, USA.
[2]Space Sciences Laboratory, University of California, Berkeley, California, USA.

rate, as photoelectrons are an important heating source in the ionosphere. Recently, *Frahm et al.* [2010] estimated the total photoelectron escape rate from Mars, yielding a value of roughly 3×10^{23} electrons/s. This estimate of photoelectron escape rate is in good agreement with the total heavy ion escape rate estimated by *Barabash et al.* [2007] using Mars Express' Ion Mass Analyzer. However, it is an order of magnitude lower than the total ion escape rate determined by *Lundin et al.* [2008], using the same ion instrument.

[6] The *Frahm et al.* [2010] study represents a break-through in calculating photoelectron escape rates and their potential as an ion escape proxy within the relatively robust superthermal electron databases. A relationship should be established between the high-altitude photoelectron measurements and corresponding photoelectron measurements in the dayside ionosphere. *Liemohn et al.* [2006a] explores this for a few case studies. However, we must also know how the ionospheric photoelectron fluxes vary with Martian atmospheric, solar radiation, and solar wind conditions. *Liemohn et al.* [2003] explored the behavior of photoelectrons trapped within the minimagnetospheres of Mars. They showed that there is a noncollisional scattering mechanism that isotropizes the higher-energy photoelectrons (above 100 eV) but not the lower-energy ones. Though, they only considered a few specific case studies from the MGS database. If we can better understand how the electrons are being created and behaving in the lower altitudes, then we can better describe the plasma environment of Mars and hopefully the atmospheric escape to deep space.

[7] The goal of this study is to examine data from the Magnetometer and Electron Reflectometer (MAG/ER) [*Acuña et al.*, 1992] instrument on MGS and to explore the factors controlling the flux of dayside photoelectrons. We compare photoelectron fluxes with different parameters, such as location, solar radiation intensity, and dynamic pressure. We determine the relative importance of each of these factors and thereby better understand the physical processes governing near-Mars space (including, indirectly, atmospheric escape).

2. Methodology

[8] This study examines photoelectrons on closed field lines associated with Mars' strong crustal magnetic field. Mars Global Surveyor has two important instruments that make this study possible, a magnetometer and an electron reflectometer. The magnetometer onboard identifies the signatures of crustal field lines and the electron reflectometer provides the data on the suprathermal electrons. We limit the study to the strong crustal field regions of the southern hemisphere when MGS consistently observes atmospheric suprathermal electrons dominated by photoelectrons. Furthermore, we are only considering the mapping phase/extended phase orbits of MGS, when the satellite was locked into a circular, Sun-synchronous orbit at 400 km altitude and 0200–1400 LT. During the aerobraking and science phasing orbits of MGS, the satellite routinely entered the ionosphere (and observed photoelectrons) across a range of latitudes, longitudes, and local times. The coverage, however, is not complete. To avoid sampling bias, only the circular orbit data will be used in this survey of the MAG/ER database. The satellite altitude of 400 km, how-

ever, is above the ionosphere most of the time. It is only over the strongest crustal field sources that the planetary magnetic field is intense enough to create a significant minimagnetosphere, allowing the ionosphere to extend up to the MGS orbit altitude.

2.1. Data Filtering

[9] The key to performing this study was accurately identifying regions of strong crustal field lines so that photoelectrons could be isolated and examined. This was done by creating a number of selection criteria that are used to identify time periods in which the desirable photoelectron data exist. These selection criteria are as follows, latitude, longitude, magnitude of the magnetic field, magnetic elevation angle (the angle relative to the local horizontal, 0 degrees being parallel Mars' surface and 90 degrees being parallel to the radial vector of Mars), and solar zenith angle.

[10] Filtering based on latitude and longitude helps isolate regions of strong crustal field lines, specifically those located in the southern hemisphere. We constrain the data we look at to a region between −30 and −70 degrees north latitude and between 160 and 200 degrees east longitude represented by the white box in Figure 1. Figure 1 shows the radial magnetic field above Mars as compiled from MGS MAG data by *Connerney et al.* [2005]. Our selection constraints limit the data included in our survey to those parts of the ionosphere dominated by the crustal fields. This helps to ensure that MGS is flying through the ionosphere and observing atmospheric photoelectrons close to their source region.

[11] Strong crustal fields are most notably associated with the enhanced magnetic magnitude. For the purpose of this study we analyze regions where the magnitude of the magnetic field is greater than 30 nT.

[12] The elevation angle of the magnetic field is also important. Our goal was to study photoelectrons on closed field lines. Therefore, it is necessary to identify and reject the cusp regions typically characterized by high magnetic elevation angles. The magnetic field becomes vertical in the cusp regions and the flux spectrum of the measured electrons changes. This change suggests that trapped photoelectrons are no longer being measured and instead, magnetosheath (i.e., solar wind) electrons are dominating the measurement. Therefore, we remove all data that have an absolute magnitude elevation angle greater than 45 degrees.

[13] Peaks of photoelectron production occur at 21–24 and 27 eV (Figure 2). These peaks are due to the ionization of carbon dioxide by the strong solar line He II at 30.4 nm [*Mantas and Hanson*, 1979]. Our study focuses on these strong peaks, specifically we used the 27 eV energy channel of the Electron Reflectometer (ER) instrument.

[14] Finally, the solar zenith angle is used to restrict measurements to sunlit times by requiring solar zenith angles less than 90 degrees. The nightside leg of the orbit is at 0200 LT, and the photoelectrons that were scattered into the trapped zone on the dayside are completely removed from minimagnetosphere by this time via a undetermined scattering or drift mechanism (at least below the detector threshold, yielding "plasma voids" in the ER data [*Mitchell et al.*, 2001]). Therefore, the unlit observations are excluded from the analysis.

[15] The process is complicated by the fact that the MGS ephemeris data such as latitude, longitude, solar zenith
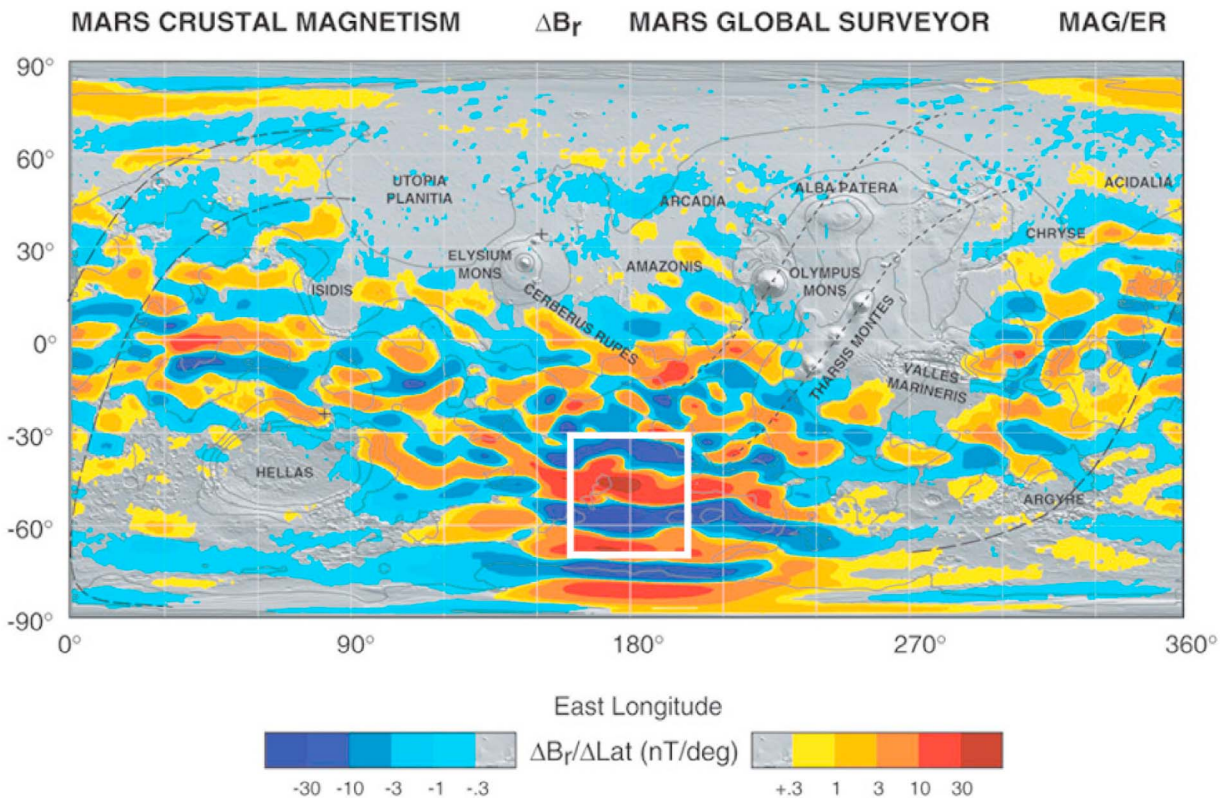
Figure 1. Radial B field of Mars [*Connerney et al.*, 2005], with the white box representing the latitudinal and longitudinal selection boundaries of this study.

angle, and positional data have a cadence of 60 s. The magnetic data have a cadence of 1 s. Therefore, we used a spline function on the ephemeris data so that it had the same time scale as the magnetic field data. This should be acceptable

Figure 2. Observed electron measurements from MGS. The cusp and sunlit crustal field measurements are from an orbit on 15 January 2004. The plasma void is from a nightside crustal field during an orbit from 15 September 1999. The other line is the modeled photoelectron spectra (scaled for illustrative purposes) [*Liemohn et al.*, 2003].

because the orbit is circular and changes in a continuous, predictable manner.

[16] Finally, due to imperfections in the filter and transient events such as Coronal Mass Ejections and flares, flux data three standard deviations away from the mean were removed. This has very little effect on the overall distribution and does not change the conclusions drawn from the results presented below.
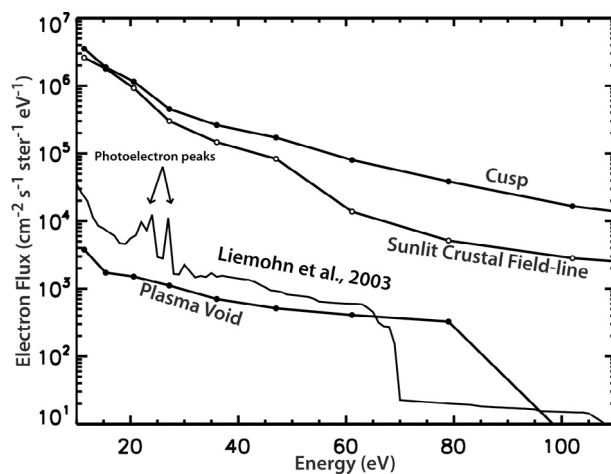
2.2. Pitch Angle

[17] Depending on the angle between the Electron Reflectometer and the local magnetic field, the instrument cannot always observe all pitch angles [see, e.g., *Liemohn et al.*, 2006a, Figure 9]. Additionally, the pitch angle distributions are not necessarily continuous, therefore taking an average is unacceptable. In order to achieve the most consistent measurement we need to consider a specific pitch angle range. Regardless of the local magnetic field, the pitch angle of 90 degrees (locally mirroring electrons) should always be observable. For the purposes of this study we used a pitch angle bin that contained electron fluxes from 80 to 90 degrees. In section 4.5 we will discuss other angle bins, which produce results that are consistent with our selected bin.

2.3. Flux Filter Data Interface

[18] In this study we used proxies to analyze other factors that influence the observed photoelectron population such
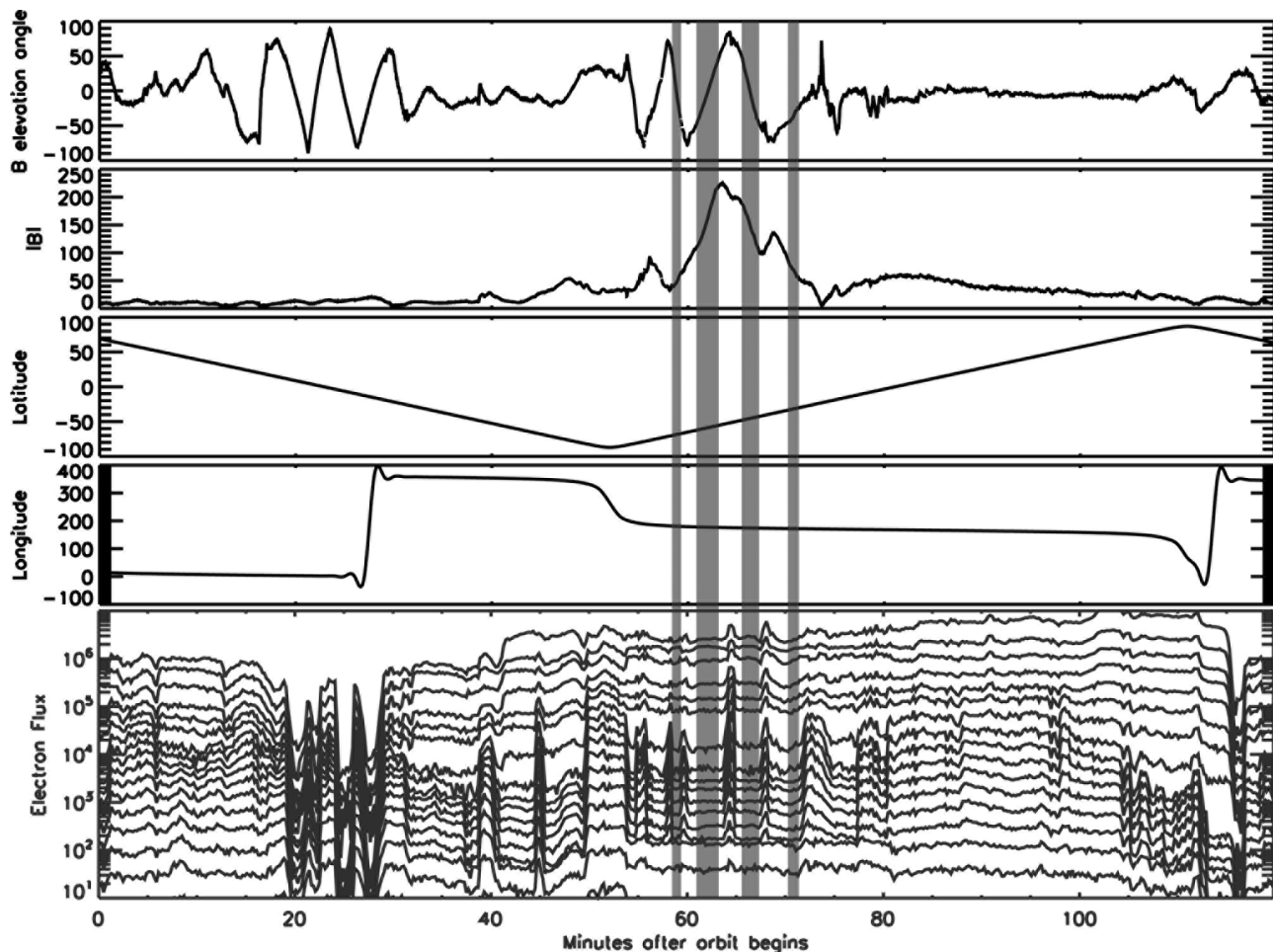
Figure 3. This is a plot of the 15 January 2004 10 h orbit. The gray vertical bars indicate times when data were collected for this study. Shown from top to bottom are magnetic elevation angle (in degrees), magnetic magnitude (nT), north latitude (in degrees), east longitude (in degrees), and the electron flux (cm^{-2} s^{-1} $ster^{-1}$ eV^{-1}) in numerous energy channels (low energy 10 eV progressing to several keV).

as solar EUV radiation and solar wind pressure. The solar EUV proxy is based on F10.7cm measurements made at Earth and scaled to Mars' orbital distance and location [*Mitchell et al.*, 2001; D. Brain, personal correspondence, 2009]. The solar wind pressure proxy is based on magnetic field measurements made at Mars as first used by *Brain et al.* [2005]. These external data sets needed to be merged with the MGS data set. The time between data points in these data sets were never less than an hour, and due to the unpredictable nature, a spline was inappropriate. Therefore, each data point in the MGS data set was paired with the nearest data point in the proxy data sets temporally.

2.4. Verification

[19] There are a number of parameters that may seem arbitrarily chosen, such as the elevation angle constraint. A method was developed to determine how effective the data selection process was. In regions magnetically linked to the lower atmosphere the electron flux in the 20–50 eV energy range is enhanced due to photoionization [*Fox and Dalgarno*, 1979; *Mantas and Hanson*, 1979; *Mitchell et al.*, 2001]. In energy ranges greater than 65 eV ionizing flux, and ionization cross sections are greatly reduced and

there is a sharp drop off in electron flux measurements (Figure 2) [*Mitchell et al.*, 2001]. This drop is due to a precipitous decrease in solar EUV flux at wavelengths less than 15 nm [e.g., *Hinteregger*, 1981] and produces a characteristic "knee" feature in the photoelectron energy spectrum in the 65–75 eV range [e.g., *Nagy and Banks*, 1970]. Therefore, the shape of the suprathermal electron flux versus energy spectrum changes depending on the environment in which the instrument is observing [e.g., *Crider et al.*, 2005; *Mitchell et al.*, 2001]: solar wind, magnetosheath, or closed crustal fields. We developed a proxy that is based on ratios of observed electron flux in different energy channels. Specifically, we focused on the sharp "knee" in the photoelectron flux near 60 eV (see Figure 2), a feature that is absent in solar wind and magnetosheath spectra. The ratio of the flux at ~27 eV to that at ~102 eV is therefore, much higher for environments where photoelectrons dominate than for the other regions. The ratio between these energy channels yields a clear identifier between what appears to be solar wind-like spectra and photoelectron dominated spectra. Through visual examination of many orbits of electron data, this "divide" occurs as the magnetic elevation approaches 45 degrees. This magnetic elevation angle constraint should
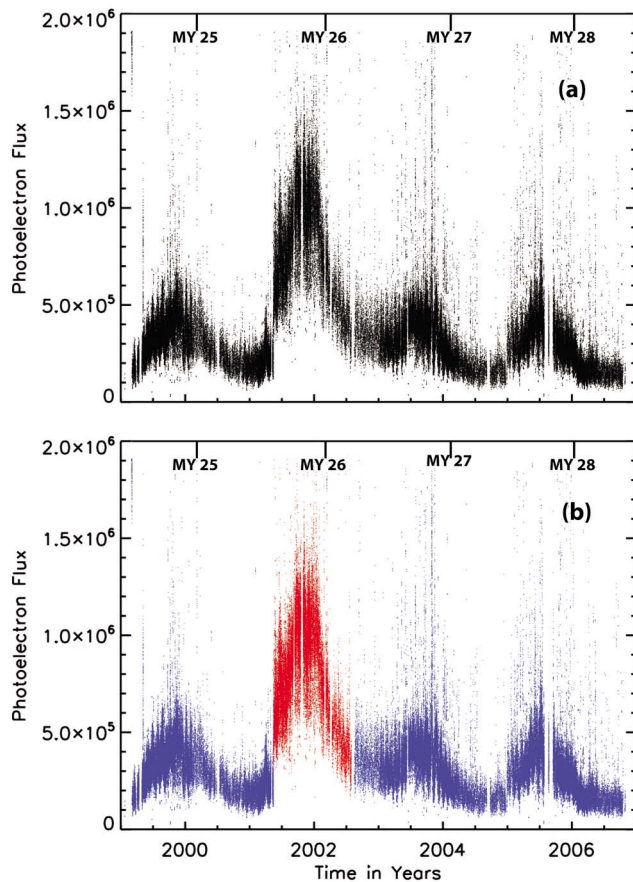
Figure 4. (a and b) Photoelectron flux (cm^{-2} s^{-1} ster^{-1} eV^{-1}) versus time. The coloring scheme in Figure 4b is used in Figures 5 and 6 to highlight the difference between this enhanced period (SS25, red) and all other times (non-SS25, blue).

remove most solar wind-like spectra measurements from the data we analyze.

[20] In summary, a number of choices were made regarding the location, characteristics of the magnetic field, and even how the data sets were aligned temporally. Figure 3 shows the magnitude and elevation angle of the magnetic field, the spacecraft latitude and longitude, and electron flux values for a selected orbit (15 January 2004 10 h). The gray vertical stripes indicate the times identified by our filter as photoelectron observations, and are included in our statistical analysis. The selected data cover about 10 min during this orbit, selected during times of low elevation angle with high background magnetic field. The bottom panel shows electron flux time series for numerous ER energy channels ranging from 11.4 to 746 eV, in which the fluxes in each channel are relatively constant during the selected observation intervals (at least on this compressed, logarithmic scale).

[21] The selected times cover about 10 min of this 120 min long orbit, and there is typically only 1 pass (sometimes 2 passes) through the selection box indicated on Figure 1 for each day. However, there are 8 years of mapping/extended phase orbits. Furthermore, the ER sensor produces a full

energy sweep distribution around the anode ring every 6 s. Taking the average of 1.3 passes per day through the selection box with 10 min per pass with 10 distributions per min over 8 years, our database of dayside crustal field photoelectrons contains over 280,000 electron flux measurements. This is a vast database that should produce statistically significant results regarding the factors controlling photoelectron fluxes at Mars.

3. Results

[22] There are a number of potential drivers for the photoelectron population on the closed crustal field lines of Mars, such as solar EUV and X-ray radiation, solar wind pressure, latitude, longitude, magnetic field strength, elevation angle of the magnetic field, and the state of the underlying atmosphere. In turn, we will examine the effect that each of these has on the photoelectron population.

3.1. Time Separation

[23] Figure 4 shows the observed photoelectrons flux versus time of the locally mirroring electrons detected by the 27 eV energy channel in our region of interest. Several expected features are seen in this time series plot, most notably the seasonal increase and decrease each Mars year. These measurements are from the southern hemisphere, and in addition to a more favorable planetary tilt during the southern summer, Mars is also significantly closer to the Sun. This causes the systematic, orbit-induced periodicity in the flux data. Increases in the photoelectron flux appear in the southern hemisphere summer of Martian years 24, 25, 26, and 27. There are many short-duration spikes superimposed on this periodicity, which are likely caused by coronal mass ejections or flares. The second of these seasonal peaks, beginning in the southern summer of Martian year 25 (SS25), appears have a much more significant enhancement of photoelectron flux than the other three summers. During this peak in late Martian year 25, the photoelectron flux is nearly doubled, as compared with the rest of the data set. We found in our analysis that this larger photoelectron flux enhancement behaves somewhat differently. Certain parameters, specifically solar radiation and the state of the underlying atmosphere, affect the photoelectron flux in unexpected ways, as is shown in sections 3 and 4.

[24] With this in mind the analysis hereinafter will be plotted using different colors, dependent on the time period in which the data was collected. Red data points will represent times when the photoelectron flux was greatly enhanced during the southern summer beginning in Mars year 25. Blue points represent all other times. These color designations are shown in Figure 4b.

3.2. Parameter Analysis

[25] Figure 5 presents a collection of scatterplots comparing the photoelectron data of Figure 4 against parameters that could influence the electron population. The trend line represents the least squares fit, whose slopes, y intercepts, and correlation coefficient are given in the Table 1.

3.2.1. EUV Radiation

[26] Figure 5a shows the EUV radiation proxy has a strong linear relationship with observed photoelectron flux. The EUV radiation proxy is calculated from the formula of
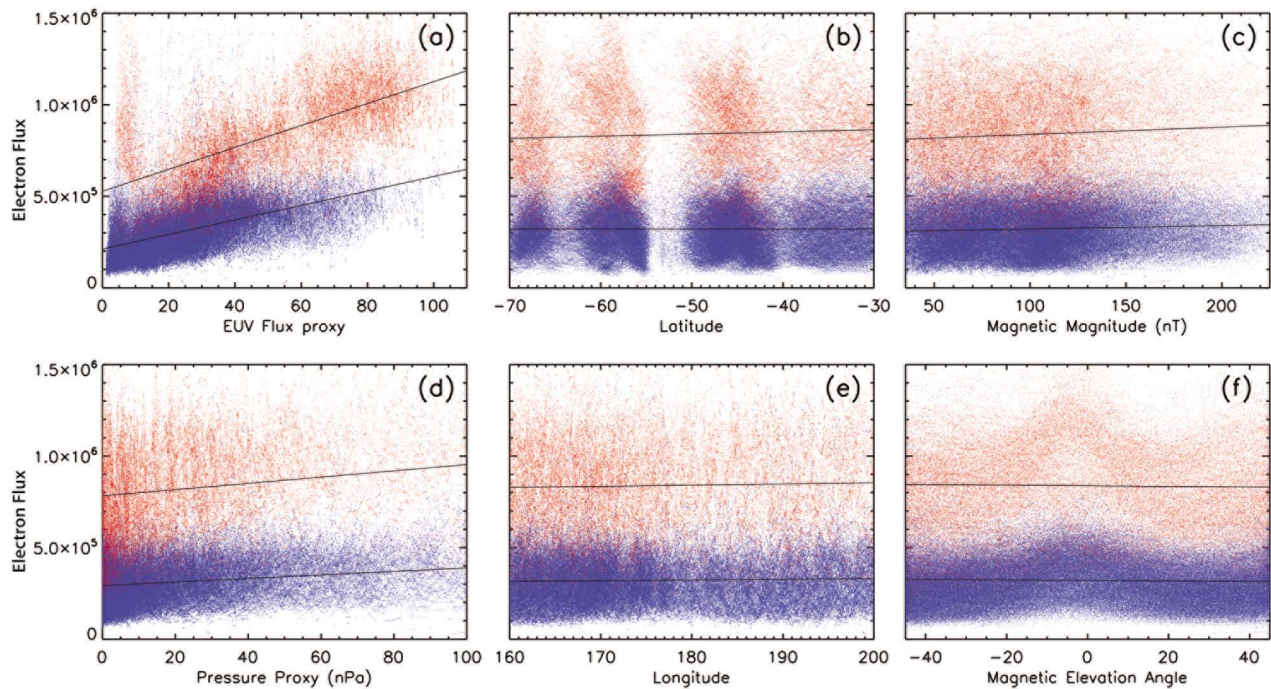
Figure 5. Each panel is a scatterplot of photoelectron flux (cm^{-2} s^{-1} $ster^{-1}$ eV^{-1}) versus a parameter: (a) EUV flux proxy, (b) latitude (degrees north), (c) magnetic magnitude (nT), (d) a solar wind dynamic pressure proxy (Pa), (e) longitude (degrees east), and (f) magnetic elevation angle (degrees). As in Figure 4b, the data in red represent the time period between mid-2001 and mid-2002, and the data in blue represent all other sampled times.

Mitchell et al. [2001], who use the F10.7 cm solar flux measurements at Earth compiled by NOAA, interpolate these solar flux measurements with a polynomial trigonometric expression depending on the Earth-Sun-Mars angle, and then reduce the value according to the Sun-Mars distance. This yields a proxy of the solar EUV flux at Mars.

[27] This flux proxy also needed to be adjusted to the specific solar zenith angle at which MGS is measuring [e.g., *Fox and Yeager*, 2006]. We approximate the atmosphere to be isothermal, to have constant gravity, and consist of only CO_2. The production of photoelectrons should be governed by the equation $P = I\sigma_i n$, where P is the production term, I is the modified solar EUV flux given by $I = I_{sun}e^{-\tau}$, I_{sun} is the solar EUV proxy unaltered, σ_i is the ionization cross section (assumed here as the cross section for the strong solar line He II at 30.4 nm), and n is the number density given by $n = n_0e^{-z/H}$. H is the scale height given by kT/mg, where k is the Boltzmann constant, T is the neutral temperature, m is

the mass of a single atom assumed to be CO_2, and g is the acceleration due to gravity. The optical depth is $\tau = \sigma_a Hn^*sec(\chi)$, where σ_a is the absorption cross section and χ is the solar zenith angle. Production maximizes when optical depth is at unity, so we set τ to unity. Therefore, maximum production is given by $P_{max}(x_{max},\chi) = I_0\ e^{-1}*\sigma_i\ /\ (H^*\sigma_a\ sec(\chi))$. Our data set includes solar zenith angles in excess of 75 degrees, therefore the Chapman Function, Ch $(Rg,\ \chi)$ [*Smith and Smith*, 1972] replaces $sec(\chi)$, where $Rg = R/H$, where R is the distance from the center of Mars. Our modified solar EUV proxy is therefore $I = I_0/\ Ch(Rg, \chi)$.

[28] There are two interesting features to point out in Figure 5a. First there appears to be two separate populations of photoelectrons. The y intercept and the slope of the red flux is significantly enhanced when compared to the blue population. A second feature to point out is that the photoelectron fluxes are elevated relative to the linear trend when the solar EUV proxy is small. This corresponds to

Table 1. Slopes, Y Intercepts, and Correlations Coefficients for Figure 5

	Southern Summer 25 (Red)			Non–Southern Summer 25 (Blue)		
	Slope	Y Intercept	Correlations Coefficients	Slope	Y Intercept	Correlations Coefficients
EUV proxy	6.0E + 03	5.3E + 05	0.59	4.0E + 03	2.1E + 05	0.5
Pressure proxy	1.7E + 03	7.8E + 05	0.33	1.0E + 03	2.9E + 05	0.33
Latitude	1.2E + 03	9.0E + 05	0.05	1.0E + 01	3.2E + 05	0.001
Longitude	6.5E + 03	7.2E + 05	0.028	3.8E + 02	2.5E + 05	0.031
B Magnitude	4.0E + 03	8.0E + 05	0.06	1.9E + 02	3.0E + 05	0.05
B Elevation	−1.7E + 02	8.4E + 05	−0.017	−1.3E + 02	3.2E + 05	−0.026

when the solar zenith angles are very high solar zenith angles (>85).

3.2.2. Solar Wind Dynamic Pressure

[29] The solar wind dynamic pressure was obtained using David Brain's proxy for solar wind pressure at Mars [*Brain et al.*, 2005]. This gives a lower-bound estimate of dynamic pressure at the subsolar point. This pressure value is then multiplied by the cosine squared of the solar zenith angle to yield the pressure normal to the planet surface assuming a flow around a sphere. Figure 5d shows the photoelectron fluxes as a function of this local radial pressure proxy. Again, there appears to be two separate populations of photoelectrons. While there does, at first, appear to be a slightly linear trend, the data appear dispersed enough to indicate a weakness in statistical significance. Table 1 shows a reduction in the correlation coefficient when compared with the solar EUV flux proxy. This is not unexpected, however, as the pressure proxy data have a two hour cadence, and pressure proxy sometimes varies significantly in between measurements (frequently by as much as 25%).

3.2.3. Magnetic Field

[30] Figure 5c presents the photoelectron flux against the local magnetic field magnitude. The flatness and low correlation coefficient of the scatterplot indicates that photoelectron flux is independent of the local magnetic field.

[31] Figure 5f shows the photoelectron flux versus the magnetic elevation angle. This study was restricted to photoelectrons on closed field lines; as described earlier, absolute elevation angles greater than 45 degrees were rejected due to the likelihood that they were open field lines (and thus the electron distribution possibly contains magnetosheath particles). Still, Figure 5f shows that there is a slight enhancement of photoelectrons near zero degrees in elevation angle. This unexpected peak in the distribution with magnetic elevation angle will be discussed in section 4.4.

3.2.4. Longitude and Latitude

[32] Longitude appears to have no significant affect on the photoelectron population (Figure 5e). The latitude, shown in Figure 5b, also appears to have little to no affect on the photoelectron population. Because of the arcade structure of the magnetic field within the selection box of this survey, there are gaps in the electron data at certain latitudes that correspond to magnetic cusps regions. Second, there is a slight enhancement of the photoelectron fluxes near the center of each "clump" of electron flux measurements. This will be discussed in further detail in sections 4.3 and 4.4.

3.3. Removing the EUV Flux Signal

[33] The effect of the EUV flux was removed to determine if there were any additional parameters that may be affecting the photoelectron flux, but too weak to be observed due to the strong EUV signal. Figure 6 shows the same information as Figure 5 with the effect of EUV flux subtracted from the overall photoelectron flux. To obtain these scatterplots, the linear fits shown in Figure 5a were subtracted from the individual photoelectron measurements (done separately for the southern summer 25 (red) and other times (blue)). Therefore, in Figure 6, the flux values can be negative (in fact, half of the values should be negative).

[34] Table 2 and Figure 6 show that some trends are altered when the signal due to EUV flux is removed. The slope of electron flux verses pressure remains noticeable,

but the correlation coefficient remains low. The localized peaks at the zero elevation angles are still seen in Figures 5b and 5f. These peaks, therefore, are not due a systematic bias between these parameters and the solar EUV radiation but exist for different reasons. Finally, when the EUV signal is removed from the latitude verse electron flux plot (Figure 6b) a new trend emerges, yet remains a relatively weak correlation (<0.30). The implications of this are discussed in section 4.

4. Discussion

[35] The dominant factor controlling the photoelectrons in the Mars dayside ionosphere explored thus far is the local EUV flux proxy. But some aspects of the photoelectron population remain unexplained. There appears to be two distinct populations of photoelectrons with different functional dependencies on EUV flux proxy. This population split, along with several other issues relating to photoelectron fluxes at Mars, will be discussed in detail.

4.1. EUV Solar Flux

[36] The presence of what appears to be two separate populations of photoelectrons is clearly seen and quantified in Figure 5a. Interestingly, the slope relating photoelectron flux to the EUV flux proxy was different in the two time periods we analyzed. The observation of different, well correlated, slopes is unique to the relationship between solar flux and photoelectron flux. There appears to be no significant influence of any other parameters we explored (Figure 6); therefore other possible causes for the separate populations of photoelectrons need to be considered.

[37] The most likely scenario was that the neutral atmosphere was somehow different during these two time periods and this was affecting the photoelectron population. This is a plausible explanation because the period of photoelectron flux enhancement is temporally restricted, starting in mid-2001 and lasting until mid-2002. If there is a plausible explanation for a change in the thermosphere during this time interval, then perhaps this can explain a change in the dependence of the photoelectron flux on the EUV flux. If the thermospheric density, temperature, and/or composition are altered, then a change in the photoelectron flux should also occur. A planetary-scale dust storm lasting several months began in August 2001. Planetary dust storms typically alter the density, temperature and composition of the lower thermosphere [*Bougher et al.*, 1997, 2006]. It is conceivable, then, that a global dust storm could alter the thermosphere at even higher altitudes, in particular in the production region of the photoelectrons above 120 km altitude.

[38] The electron flux change is a result of a new relationship between the energy dependant production and loss of photoelectrons. Enhancements in thermospheric densities would tend to alter the rate of photoelectron production and loss, possibly creating the enhanced relationship between solar flux and photoelectron flux observed in late Mars year 25. *Forbes et al.* [2008] showed that there was a sizable increase in the exospheric temperature and densities during this enhanced period, but also showed moderately increased temperatures and densities during other periods. Another possible explanation for the changed balance between production and loss could be a chemical composition change in
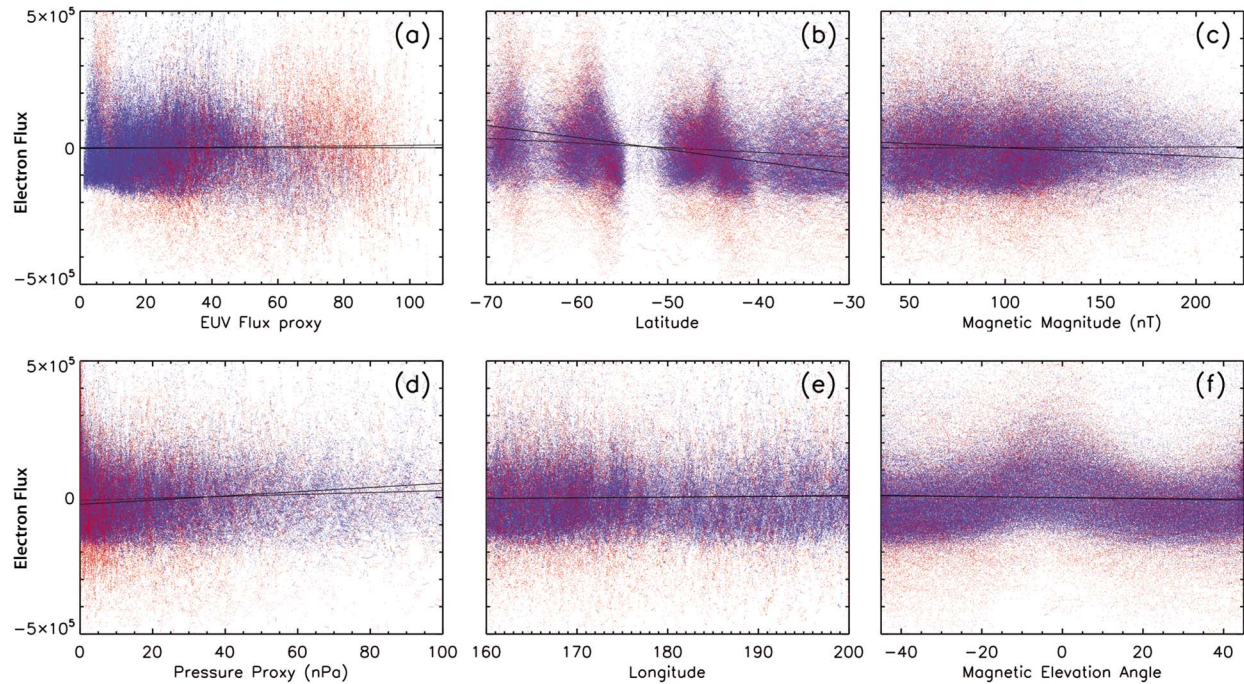
Figure 6. Same as Figure 5 with the signal due to solar EUV proxy removed. Each panel in Figure 6 shows photoelectron flux (cm^{-2} s^{-1} $ster^{-1}$ eV^{-1}) with the average linear trend due to solar EUV proxy removed versus one of the considered parameters: (a) EUV flux proxy, (b) latitude (degrees north), (c) magnetic magnitude (nT), (d) solar wind dynamic pressure proxy (Pa), (e) longitude (degrees east), and (f) magnetic elevation angle (degrees). As in Figure 4b, the data in red represent the time period between mid-2001 and mid-2002, and the data in blue represent all other sampled times.

the production region functioning similar to O/N_2 ratios in the Earth's ionosphere [*Fuller Rowell et al.*, 1994]. Changing composition could affect the number of neutrals that are ionized by slightly altering the intensity of EUV flux due to increased (or decreased) photoabsorption or photo-ionization of different species. Even if production is unaffected, altering the altitude of the production region would alter the loss due to changes in the total scattering along the electron's path from the production region to 400km. In fact, *Fox* [2004] compares solar minimum conditions to solar maximum conditions and determines that during solar max the altitude and the production of photoelectrons increases during enhanced soft X-rays. Determining the exact cause for the changed slope in Figure 5a is difficult at this time, but it is certainly worthy of attention and further study.

[39] Let us further examine the change of the slope of the relationship between the photoelectron fluxes and the EUV radiation. The results discussed thus far are for locally mirroring electrons, indicating that the altitude observation (400 km) is the lowest extent of their bounce path. This means that the electrons were produced in the source region (~120 km) then transported along the magnetic field lines to higher altitudes. Then some scattering or drift mechanism must have altered the electrons pitch angle so that the electrons are locally mirroring at 400 km. The result of this scattering is that these particles no longer come into contact with their source region in the lower thermosphere (until the electrons are scattered again or drift). Therefore the change in slope could also be due to change in scattering above 400 km altitude. Further study will also be needed to determine if high altitude scattering plays a significant role in the altered slopes observed in Figure 5a.

Table 2. Slopes, Y Intercepts, and Correlations Coefficients for Figure 6

	Southern Summer 25 (Red)			Non–Southern Summer 25 (Blue)		
	Slope	Y Intercept	Correlations Coefficients	Slope	Y Intercept	Corrrelations Coefficients
EUV proxy	4.8E + 00	−4.5E + 02	0	1.2E + 02	−2.8E + 03	0.017
Pressure proxy	7.8E + 02	−2.5E + 04	0.18	3.5E + 02	−1.0E + 04	0.136
Latitude	−4.4E + 03	−2.3E + 05	−0.236	−1.7E + 03	−8.5E + 04	−0.1548
Longitude	2.5E + 02	−4.4E + 04	0.013	2.9E + 02	−5.1E + 04	0.02754
B Magnitude	3.1E + 02	3.1E + 04	0.0619	2.5E + 01	−2.1E + 03	0.0083
B Elevation	−2.0E + 02	−6.0E + 02	−0.024	−1.3E + 02	2.1E + 02	−0.029

[40] Note that *Lillis et al.* [2008] also considered the influence of this global dust storm on the thermosphere and electron transport. They considered the nightside MGS MAG/ER observations (again, like this study, over the entire mapping/extended phase mission) of precipitating solar wind/magnetosheath electrons and the backscatter and loss of these particles within the thermosphere. In a series of simulations, they precipitated the observed downflowing electrons into their calculation domain. They then altered the thermospheric density until the simulated upflowing (i.e., reflected) electron fluxes matched the observed values. The resulting best fit thermospheric density has a significant peak during this global dust storm, although the peak density is nearly the same (within 20%) corresponding peaks at this same seasonal time for the other Mars years [see *Lillis et al.*, 2008, Figure 11]. Our conclusion is consistent with the finding from *Lillis et al.* [2008], although the thermospheric density change (or, at least, the resulting change in the electron flux dependence on solar radiation) is probably larger on the dayside than on the nightside.

[41] Also, a noticeable enhancement of photoelectron flux occurs at very low values of solar EUV proxy (see Figure 5a). Analysis indicated that these points had very high solar zenith angles in excess of 85 degrees. The tilt of Mars in the southern summer allows high latitudes to be continuously sunlit, and this enhancement appears to be emerging from sunlit nighttime passes of the spacecraft. Due to near continuous production, these measurements are enhanced relative to what would normally be expected from such high solar zenith angles.

4.2. Solar Wind Dynamic Pressure

[42] Originally (Figure 5d), solar wind pressure appears to have an influence on the photoelectron flux, and when the signal due to solar EUV flux is removed (Figure 6d), the influence of pressure on photoelectron flux is still present. While we cannot discount the contribution of solar pressure, the uncertainty in the pressure proxy data makes drawing conclusions difficult. The region we are exploring has very strong crustal fields and it is possible that the solar wind pressure cannot easily influence this region, thus creating the observed spread in Figures 5d and 6d and low correlation coefficients in Tables 1 and 2. An additional problem is that a pressure estimate is made once per orbit (about two hours), while the pressure proxy can change significantly over that time (frequently by more than 25%). Either of these factors could be contributing to the uncertainty seen in Figures 5d and 6d, and make drawing any definitive conclusions difficult.

4.3. Longitude and Latitude

[43] Longitude appears to have no effect, photoelectron fluxes. The region examined is longitudinally uniform due to the location of the east–west oriented magnetic field arcades. Therefore, photoelectron flux is not affected uniquely by the longitude of the observation.

[44] With solar flux being a strong driver it is surprising not to see decreasing electron fluxes in the pole ward direction in Figure 5b. Besides the slight enhancement near the middle of the field lines there appears to be a nearly zero slope in Figure 5b. When the signal due to solar EUV was removed in Figure 6b, a weak trend possibly emerges (a negative one, with slightly higher electron fluxes at high latitudes). The precise explanation as to why this occurs remains elusive at this point.

4.4. Elevation Angle

[45] The magnetic field elevation angle also shows a slight enhancement near zero degrees. There are a variety of possible explanations for this observation. The field lines with zero elevation angles are the shortest field lines. These field lines would have the smallest "flux tube volume" to fill and therefore the photoelectron fluxes could be slightly enhanced. These small field lines would also have a smaller trapped zone and are quicker to "fill" with electrons. In addition, these flux tubes are the deepest that MGS observed within the magnetic arcade structures, and therefore the most protected from externally driven loss processes. Any (or all) of these explanations could be responsible for the slight increase in flux at zero elevation angle.

4.5. Other Energy Channels and Pitch Angles

[46] This study focused on a single locally mirroring pitch angle bin and the 27 eV energy channel, but other pitch angle bins and photoelectron energy channels showed similar results. The analysis presented in section 3 is only for a single energy channel and pitch angle bin. The MGS ER instrument, however, has 16 anode sectors and energy channels spanning the entire photoelectron energy range (up through the Auger electron peaks at 300 and 500 eV [*Mitchell et al.*, 2000]). A further analysis was conducted for several other energy channels (~20 to 313 eV, see Figure 7) and pitch angle bins (derived from the anode sectors), finding similar relationships between the photoelectron fluxes and these parameters; that is, for every energy and pitch angle considered in the photoelectron range 20–50 eV, the photoelectron flux had an enhanced linear relationship with the EUV flux proxy during SS25, a weak linear relationship with pressure, and essentially no dependence for all of the other parameters explored.

[47] Figure 7 shows the ratio of the slopes (calculated from linear fits of the solar flux proxy to electron flux) between the SS25 (red) and non-SS25 (blue) time periods for an expanded set of angle bins and energy channels than was seen in Figure 5a. The correlation coefficient of the fitted slopes begins near 0.6 (at 20 eV) and slowly decreases to 0.4 (300 eV) with one exception. The large spike in the ratios in the 61 and 79 eV energy bins corresponds to a reduction in the correlations coefficient of less than 0.4 for the 61 eV energy channel and less than 0.3 for the 79 eV energy channel. One likely explanation is the proximity (in eV) to the knee seen in Figure 2, and the low energy resolution of the ER sensor ($\Delta E/E = 0.25$). The ER sensor may be sensing electrons from both sides of the knee, causing a high variance in flux measurements and the low correlations coefficients calculated. In addition, differences in spacecraft charging could be shifting the spectrum relative to the MGS ER energy channels. In the energy channels where photoelectrons dominate the suprathermal electron population, from 20 to 60 eV, the slope is enhanced by about 50% in the 80–100 and 30–60 pitch angle degree bins, and about 25% in the 120–150 pitch angle bin. This indicates that the slope
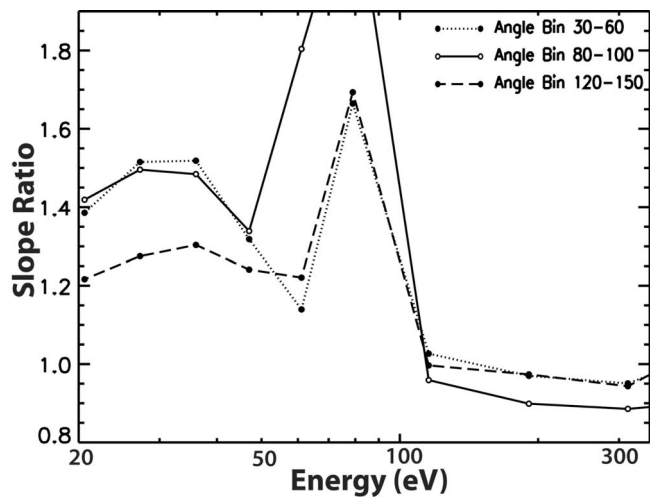
Figure 7. Ratio of the enhanced (SS25, red in Figure 4b) fitted slope to the unenhanced (non-SS25, blue in Figure 4b) fitted slope for three pitch angle bins versus energy in the solar EUV versus photoelectron flux plots as seen in Figure 5a. Energy channels shown in eV are 20.6, 27.2, 36, 47, 61, 79, 115.594, 190.935, and 313.584.

enhancement observed during Mars year 25 exists, to a varying degree, in the other pitch angle bins and photoelectron energy channels.

5. Conclusion

[48] A survey of the dayside photoelectron observations within the MGS MAG/ER database was conducted to assess the relative importance of several factors that might control photoelectron flux intensities. A stringent selection criterion was applied to identify only those electron measurements that are along the strong crustal fields that should be dominated by photoelectrons. From 8 years of mapping/extended phase MGS orbits, over 280,000 electron distributions were identified that are clearly sunlit crustal field lines containing photoelectron spectra. The results focused on a single energy channel and pitch angle bin, but all other energy channels and pitch angle bins dominated by photoelectrons have a similar relationship as the one shown.

[49] The main conclusion is that solar EUV radiation and the state of the underlying atmosphere are the major factors that control the flux of dayside ionospheric photoelectrons. The dependence of photoelectron flux on solar EUV was expected, but finding that during different time periods (specifically late Mars year 25 versus all other times) the relationship between photoelectron fluxes and the EUV radiation changes was surprising. The enhanced dependence of photoelectron flux in relation to solar EUV occurs during a global dust storm lasting several months. The implication is that the dust storm altered the atmosphere all the way up through the thermosphere and greatly enhanced the production rate of photoelectrons in their source region and at higher altitudes of the Martian ionosphere, while also potentially changing the loss rate of the photoelectrons. During the period when the dust storm was present on Mars (SS25) the photoelectron flux was observed to nearly double relative to other periods observed by MGS. Because pho-

toelectrons and photoions can be important in a variety of escape mechanisms a further study of this phenomenon could be relevant to a number of estimates of atmospheric escape at Mars.

[50] There is also a slight influence due to the elevation angle of the local magnetic field, with the flux increasing slightly near zero elevation angle (i.e., horizontal field). It is important to note that any trend emerging from the elevation angle of the local magnetic field is significantly less influential than solar EUV trend.

[51] Photoelectron fluxes were also shown to be independent of latitude. One would expect measurements closer to the poles to have lower photoelectron fluxes due to generally higher solar zenith angles, and Figure 5b (the latitude dependence before the EUV proxy is subtracted) shows this is not the case. Further study must be performed to determine the cause of this phenomenon.

[52] Finally, the influence of the solar wind dynamic pressure on the photoelectron fluxes within these closed magnetic field lines is negligible within statistical uncertainties.

[53] All of these findings have implications for eventually quantifying atmospheric loss from electron measurements. This study has compared the 400 km altitude photoelectron flux dependence on various controlling factors, in particular showing an interesting relationship between photoelectron flux, the local EUV radiation, and the state of the atmosphere. Further study of this relationship could help develop a link between high-altitude photoelectron observations, ionospheric conditions, and perhaps even ionospheric outflow rates.

References

Acuña, M. H., et al. (1992), Mars Observer magnetic fields investigation, *J. Geophys. Res.*, *97*(E5), 7799–7814, doi:10.1029/92JE00344.

Barabash, S., et al. (2007), Martian atmospheric erosion rates, *Science*, *315*, 501–503, doi:10.1126/science.1134358.

Bougher, S. W., J. Murphy, and R. M. Haberle (1997), Dust storm impacts on the Mars upper atmosphere, *Adv. Space Res.*, *19*(8), 1255–1260, doi:10.1016/S0273-1177(97)00278-0.

Bougher, S. W., J. M. Bell, J. R. Murphy, M. A. Lopez-Valverde, and P. G. Withers (2006), Polar warming in the Mars thermosphere: Seasonal variations owing to changing insolation and dust distributions, *Geophys. Res. Lett.*, *33*, L02203, doi:10.1029/2005GL024059.

Brain, D. A., J. S. Halekas, R. J. Lillis, D. L. Mitchell, R. P. Lin, and D. H. Crider (2005), Variability of the altitude of the Martian sheath, *Geophys. Res. Lett.*, *32*, L18203, doi:10.1029/2005GL023126.

Carr, M. H., and G. G. Schaber (1977), Martian permafrost features, *J. Geophys. Res.*, *82*(28), 4039–4054, doi:10.1029/JS082i028p04039.

Chassefiere, E., and F. Leblanc (2004), Mars atmospheric escape and evolution: Interaction with the solar wind, *Planet. Space Sci.*, *52*, 1039–1058, doi:10.1016/j.pss.2004.07.002.

Connerney, J. E. P., M. H. Acuña, N. F. Ness, G. Kletetschka, D. L. Mitchell, R. P. Lin, and H. Reme (2005), Tectonic implications of Mars crustal magnetism, *Proc. Natl. Acad. Sci. U. S. A.*, *102*(42), 14,970–14,975., doi:10.1073/pnas.0507469102.

Crider, D. H., J. Espley, D. A. Brain, D. L. Mitchell, J. E. P. Connerney, and M. H. Acuna (2005), Mars Global Surveyor observations of the Halloween 2003 solar superstorm's encounter with Mars, *J. Geophys. Res.*, *110*, A09S21, doi:10.1029/2004JA010881.

Forbes, J. M., F. G. Lemoine, S. L. Bruinsma, M. D. Smith, and X. Zhang (2008), Solar flux variability of Mars' exosphere densities and temperatures, *Geophys. Res. Lett.*, *35*, L01201, doi:10.1029/2007GL031904.

Fox, J. L. (2004), Response of the Martian thermosphere/ionosphere to enhanced fluxes of solar soft X-rays, *J. Geophys. Res.*, *109*, A11310, doi:10.1029/2004JA010380.

Fox, J. L., and A. Dalgarno (1979), Ionization, luminosity, and heating of the upper atmosphere of Mars, *J. Geophys. Res.*, *84*(A12), 7315–7333, doi:10.1029/JA084iA12p07315.

Fox, J. L., and K. E. Yeager (2006), Morphology of the near-terminator Martian ionosphere: A comparison of models and data, *J. Geophys. Res.*, *111*, A10309, doi:10.1029/2006JA011697.

Frahm, R. A., et al. (2006a), Carbon dioxide photoelectron energy peaks at Mars, *Icarus*, *182*, 371–382, doi:10.1016/j.icarus.2006.01.014.

Frahm, R. A., et al. (2006b), Locations of atmospheric photoelectron energy peaks within the Mars environment, *Space Sci. Rev.*, *126*, 389–402, doi:10.1007/s11214-006-9119-5.

Frahm, R. A., et al. (2010), Estimation of the escape of photoelectrons from Mars in 2004 liberated by the ionization of carbon dioxide and atomic oxygen, *Icarus*, *206*, 50–63, doi:10.1016/j.icarus.2009.03.024.

Fuller-Rowell, T. J., M. V. Codrescu, R. J. Moffett, and S. Quegan (1994), Response of the thermosphere and ionosphere to geomagnetic storms, *J. Geophys. Res.*, *99*(A3), 3893–3914, doi:10.1029/93JA02015.

Hinteregger, H. E. (1981), Representations of solar EUV fluxes for aeronomical applications, *Adv. Space Res.*, *1*(12), 39–52, doi:10.1016/0273-1177(81)90416-6.

Jeans, J. H. (1904), *The Dynamical Theory of Gases*, Cambridge Univ. Press, Cambridge, U. K.

Kar, J., K. K. Mahajan, and R. Kohli (1996), On the outflow of O_2^+ ions at Mars, *J. Geophys. Res.*, *101*(E5), 12,747–12,752, doi:10.1029/95JE03526.

Liemohn, M. W., D. L. Mitchell, A. F. Nagy, J. L. Fox, T. W. Reimer, and Y. Ma (2003), Comparisons of electron fluxes measured in the crustal fields at Mars by the MGS magnetometer/electron reflectometer instrument with a B field–dependent transport code, *J. Geophys. Res.*, *108*(E12), 5134, doi:10.1029/2003JE002158.

Liemohn, M. W., et al. (2006a), Numerical interpretation of high-altitude photoelectron observations, *Icarus*, *182*, 383–395, doi:10.1016/j.icarus.2005.10.036.

Liemohn, M. W., Y. Ma, R. A. Frahm, X. Fang, J. U. Kozyra, A. F. Nagy, J. D. Winningham, J. R. Sharber, S. Barabash, and R. Lundin (2006b), Mars global MHD predictions of magnetic connectivity between the dayside ionosphere and the magnetospheric flank, *Space Sci. Rev.*, *126*, 63–76, doi:10.1007/s11214-006-9116-8.

Lillis, R. J., S. W. Bougher, D. L. Mitchell, D. A. Brain, R. P. Lin, and M. H. Acuña (2008), Continuous monitoring of nightside upper thermospheric mass densities in the Martian southern hemisphere over 4 Martian years using electron reflectometry, *Icarus*, *194*, 562–574.doi:10.1016/j.icarus.2007.09.031.

Luhmann, J. G., and J. U. Kozyra (1991), Dayside pickup oxygen ion precipitation at Venus and Mars: Spatial distributions, energy deposition and consequences, *J. Geophys. Res.*, *96*(A4), 5457–5467, doi:10.1029/90JA01753.

Luhmann, J. G., R. E. Johnson, and M. H. G. Zhang (1992), Evolutionary impact of sputtering of the Martian atmosphere by O^+ pick-up ions, *Geophys. Res. Lett.*, *19*, 2151–2154, doi:10.1029/92GL02485.

Lundin, R., S. Barabash, M. Holmström, H. Nilsson, M. Yamauchi, M. Fraenz, and E. M. Dubinin (2008), A comet-like escape of ionospheric plasma from Mars, *Geophys. Res. Lett.*, *35*, L18203, doi:10.1029/2008GL034811.

Mantas, G. P., and W. B. Hanson (1979), Photoelectron fluxes in the Martian ionosphere, *J. Geophys. Res.*, *84*(A2), 369–385, doi:10.1029/JA084iA02p00369.

McElroy, M. B., and T. M. Donahue (1972), Stability of the Martian atmosphere, *Science*, *177*, 986–988, doi:10.1126/science.177.4053.986.

Mitchell, D. L., R. P. Lin, H. Rème, D. H. Crider, P. A. Cloutier, J. E. P. Connerney, M. H. Acuña, and N. F. Ness (2000), Oxygen auger electrons observed in Mars' ionosphere, *Geophys. Res. Lett.*, *27*, 1871–1874, doi:10.1029/1999GL010754.

Mitchell, D. L., R. P. Lin, C. Mazelle, H. Rème, P. A. Cloutier, J. E. P. Connerney, M. H. Acuna, and N. F. Ness (2001), Probing Mars' crustal magnetic field and ionosphere with the MGS Electron Reflectometer, *J. Geophys. Res.*, *106*(E10), 23,419–23,427, doi:10.1029/2000JE001435.

Nagy, A. F., and P. M. Banks (1970), Photoelectron fluxes in the ionosphere, *J. Geophys. Res.*, *75*(31), 6260–6270, doi:10.1029/JA075i031p06260.

Rossbacher, L. A., and S. Judson (1981), Ground ice on Mars: Inventory, distribution and resulting landforms, *Icarus*, *45*, 39–59, doi:10.1016/0019-1035(81)90005-1.

Smith, F. L., III, and C. Smith (1972), Numerical evaluation of Chapman's grazing incidence integral ch (X, χ), *J. Geophys. Res.*, *77*(19), 3592–3597, doi:10.1029/JA077i019p03592.

J. Frank, M. Liemohn, and M. Trantham, Department of Atmospheric, Oceanic, and Space Sciences, University of Michigan, 2455 Hayward St., Ann Arbor, MI 48109, USA. (fractaljf@gmail.com; liemohn@umich.edu; mtrantha@umich.edu)

D. Mitchell, Space Sciences Laboratory, University of California, 7 Gauss Way, Berkeley, CA 94720-7450, USA. (mitchell@ssl.berkeley.edu)